Transparent Welding of Dielectric Materials: Road to Large-Scale, High-Strength and Low Residual Shear Stress Assemblies

Manon Lafargue[1,2], Théo Fillez[1], Théo Guilberteau[1,3], Bastien Gavory[2], Michael Jarwitz[1], John Lopez*[1], and Inka Manek-Hönninger[1]

[1] *Université de Bordeaux - CNRS - CEA, CELIA UMR5107, 43 rue Pierre Noailles, Domaine du Haut-Carré, Bât. C6, 33405 Talence, France*
[2]*Amplitude, 11 avenue de Canteranne, Cité de la Photonique, 33600 Pessac, France*
[3]*Alphanov, rue François Mitterrand, 33400 Talence, France*
**Corresponding author's e-mail: john.lopez@u-bordeaux.fr*

Transparent welding of dielectric materials using ultrafast lasers is a highly promising method for glue-free glass assembling. However, dielectric materials are brittle and heat sensitive, so any high thermal gradients should be avoided during the welding process, otherwise residual stress and cracks may occur. We report on large-scale (up to 2") and high mechanical strength transparent welding of fused silica glass using a femtosecond laser source emitting 500 fs pulses at 1030 nm. Laser parameters, focusing conditions and laser trajectory are set in order to get a crack-free bulk modification and a stable weld seam. The results are characterized in terms of shear strength (up to 1 GPa) and residual stress. This latter is assessed based on the photoelastic effect, using a 6-steps phase-stepping method according to Patterson & Wang to evaluate the stress-induced birefringence in the samples with a circular polarimeter. This work opens the road to large-scale optical components assembly.
DOI:10.2961/jlmn.2026.03.3001
Keywords: femtosecond, glass welding, laser-induced birefringence, residual stress, shear strength

1. Introduction

Transparent welding of dielectric materials using ultrafast lasers is highly interesting for glue-free glass assemblies with long-term stability in photonics, microfluidics, or medical devices. The principle of transparent welding is to focus the laser beam at the interface of two glass substrates in order to heat the material thanks to non-linear absorption, and to create a molten pool, which produces a strong bonding after cooling [1]. The criteria for glass assemblies depend on the application, so it could be for example airtightness for microfluidics [2], or mechanical resistance and the capacity to act as a heat-sink for high power laser manufacturing. However, the welded area is quite often below 1 cm² [3-5], and welding over a large area (more than 1 inch) is still a challenge.

The quality of glass welding is closely linked to the extend and the location of the heat-affected zone (HAZ) which depends on the laser parameters as well as the focusing parameters [6-8]. Indeed, the HAZ increases while increasing the repetition rate or pulse energy and decreasing the scanning speed [6]. A comprehensive study of the bulk modification, as a function of scanning speed and pulse energy, has been carried out by Lafargue et al. [9]. This latter study demonstrates that process windows for transparent welding are significantly reduced in MHz- and GHz-burst modes compared to repetitive single pulse mode. Indeed, in burst mode the intensity of the main pulse is divided into several tenths or hundredths of sub-pulses in the burst, so the prefocal non-linear absorption decreases and the thermal gradient nearby the focus increases [10], which favorizes crack appearance [9]. Moreover, the energy deposition location moves upward with increasing pulse energy due to prefocal non-linear absorption [2]. The focus location has to be set in order to maximize the melted area at the interface [2]. Intensity modulation is proposed to improve the welding seam stability and to avoid an upward focus shift as observed with picosecond pulses [11].

Furthermore, the rapid heating and cooling of the glass during transparent welding induces a high thermal gradient that dramatically increases the risk of crack appearance, especially at the beginning of the weld seam when the glass is cold and brittle [6]. However, pulse after pulse, the temperature of the glass increases, and the glass becomes ductile when the steady state temperature reaches the softening temperature. So, cracks may disappear after a few ten thousand pulses, as shown in Miyamoto et al. [6]. Therefore, the beginning, and the end to a lesser extent, of the weld seam are the main weak points along the laser trajectory. Another crucial point is the airgap at the interface. Ideally, there is no airgap at the interface, so the cooling of the glass occurs with a solid surrounding material. This configuration produces a residual compressive stress, which results in a much higher mechanical resistance compared to the case of a residual tensile stress that appears when there is a narrow airgap [7].

It is well established that the macroscopic behavior of a brittle material, such a silicate glass, is determined by the weakest link, i.e., the largest defect into the material [12]. Furthermore, from Frenkel's model it is known that the theoretical shear strength of a defect-free material is estimated as the shear modulus (31 GPa for Corning 7980 fused silica) divided by 2π [13]. So, the maximum theoretical value for the shear strength of fused silica is around 4.9 GPa. This value is far above shear strengths reported in the scientific literature after glass welding [2,8,14-18]. For instance, Alexeev et al. have obtained 200 to 600 MPa on sodalime glass [14], and Sun et al. have measured 60 MPa on fused silica [2]. So, the mechanical resistance is one limitation for glass assemblies based on transparent welding with ultrafast lasers.

Several techniques have been developed for assessing the material integrity and the residual stress in a glass material, including digital image correlation, electronic speckle pattern interferometry or digital holographic imaging [19]. While these methods can provide valuable insights, they often involve complex and expensive instrumentation, and generally require slow acquisition times. Photoelastic methods offer an attractive alternative for transparent materials. They are based on the measurement of stress-induced birefringence, which manifests as an optical retardation between the ordinary and extraordinary polarization components [19]. For example, using the six-step phase-stepping method proposed by Patterson & Wang [20] with a monochromatic circular polarimeter enables the pixel-wise reconstruction of the optical retardation δ and the optical axis orientation θ, as well as the computation of birefringence and residual stress.

In this paper, we report on large-scale (up to 2”) and high mechanical strength transparent welding of fused silica using a femtosecond laser source. Welded samples were characterized in terms of shear strength and laser-induced birefringence, which was used to estimate the residual stress.

2. Materials and methods

2.1 Micromachining workstation for glass welding

The experimental setup for glass welding consists of a Yb-doped femtosecond laser (Tangor 100, Amplitude, wavelength: 1030 nm, pulse duration: 500 fs) and a homemade micromachining workstation which includes a x2 beam expander, a 2-axis galvo scanner (LS-scan 20, Lasea) equipped with a 30 mm telecentric focusing lens and mounted on a Z-axis motorized stage, and a monolithic motorized stage (Alio Industries) utilized as XY-axis for positioning and moving the sample under the laser beam. The effective numerical aperture was 0.20. The spot size was measured in air to be 6.0 ± 0.2 µm. The samples were mounted in a homemade clamping tool that applies a uniform force at the periphery of the sample assembly. A top-view vision device equipped with a microscope objective (Mitutoyo, NIR plan APO, 10X, NA 0.26) was used for positioning, for flatness setting, and for determining the interface location between the two glass samples. The moving of the samples during the welding process to generate the welding trajectory was realized with the XY-motorized stages (not with the galvo scanner) in order to cover a large processing field and to avoid any beam deformation due to working at the edges of the scan field.

The applied laser trajectory was an outward spiral pattern, either full or annular, to minimize the number of weak points along the welding seam (i.e., one starting point, one ending point). The pitch of the spiral was set to 75 µm in order to have a HAZ lateral overlap between two subsequent turns in the spiral over 2/3 of the bulk modification height. For the larger spirals with a diameter of 2 inches, each spiral turn was decomposed into 40 linear segments to simplify the trajectory and maximize the scanning speed.

The operating parameters for glass welding were adjusted according to the process windows reported in Lafargue et al. [9]. Therefore, the repetition rate was set to 200 kHz and the scanning velocity to 10 mm/s. The pulse energy was set to 51 µJ. This specific set of parameters produces a stable welding seam without any cracks. The bulk modification has a teardrop shape that results from the energy deposition location upstream the focus and subsequent heat diffusion. Tiny bubbles, which come from the thermal decomposition of fused silica under high temperature, are observed at the top of the teardrop. With this set of parameters, the width of the HAZ is about 125 µm for a single track and the height of the bulk modification is about 500 µm. The focus location was set 600 µm below the interface to compensate for the focal shift and prefocal absorption in the material. By this means, the bubbles in the bulk modification are located far from the interface of the assembly (more than 150 µm).

Welding experiments were carried out on fused silica samples (Corning 7980) with a diameter of 2 inches and a thickness of 10 mm, and with an anti-reflective coating on both sides for large-scale welding, and on fused silica samples with a diameter of 1 inch and a thickness of 3 mm for the mechanical tests. These samples are thick enough to avoid any bending while clamping at the periphery. Sample surfaces were cleaned with ethanol and a dry air jet before assembling. As explained before, a close contact between the samples (i.e., a good molecular bonding) to avoid any airgap is required before laser treatment in order to avoid tensile residual stress in the weld seam and to keep a high transparency outside the welded area (Fig. 1).

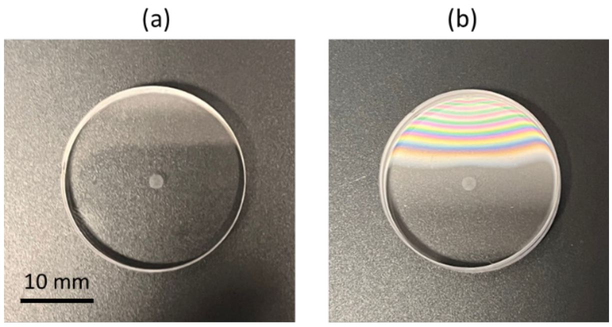

Fig. 1. Assembly of two fused silica samples with a diameter of 1 inch and a thickness of 3 mm after welding with (a) no airgap and (b) a 2 µm airgap.

2.2 Monochromatic circular polarimeter

The experimental setup for the measurements of the laser-induced residual stresses is based on a homemade monochromatic circular polarimeter as depicted in Figure 2. This device is designed for full-field stress analysis in transparent materials using phase retardation measurements. The optical configuration allows quantitative mapping of the phase retardation using a phase-stepping method based on the six-step method described by Patterson and Wang [20]. The polarimeter includes the following elements (from left to right in Fig. 2): a light-emitting diode (M530L4 Thorlabs) emitting at 522 nm provides a quasi-monochromatic illumination. It is collimated using a dedicated optic (SM2F32-A Thorlabs) to ensure uniform beam quality. The beam passes through a fixed linear polarizer (P1) that defines a well-known input polarization state. Then, a first quarter-wave plate (QWP1) is placed after the first polarizer (P1) to generate circularly polarized light, which interacts with the birefringent sample. The birefringent sample modifies the polarization state of the light due to internal stress-induced birefringence. To analyze the changes in the polarization state, several defined phase shifts are applied to the light transmitted through the sample. Therefore, a second quarter-wave plate (QWP2), mounted on a motorized rotation stage (K10CR1/M Thorlabs), is placed after the sample, followed by a half-wave plate (HWP), also motorized (K10CR1/M Thorlabs) to ensure precise and repeatable angular positioning. To image the sample plane onto the camera, an imaging system consisting of two 100 mm focal length lenses positioned at both ends of the imaging system is used. Between them, a set of two additional lenses can be inserted, consisting of a divergent lens with a focal length of −100 mm and a convergent lens of 200 mm. This configuration enables multiple magnification modes (x2, x0.5 and x1), depending on the order they are inserted. A fixed linear analyzer P2 (crossed with the input polarizer (P1)) is placed in front of the CMOS camera (Basler acA1920), positioned in the image plane, which captures the transmitted intensity for each angular configuration with pixel-level resolution. This configuration deviates slightly from a classical circular polarimeter [20] because the half-wave plate was chosen to compensate for errors introduced by rotating the analyzer (P2) [21].

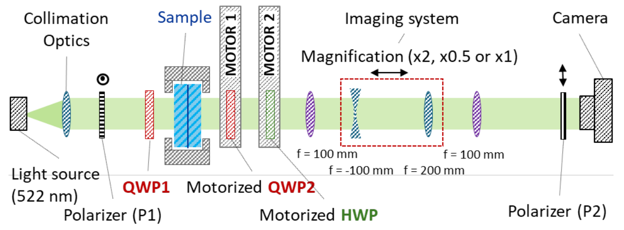

Fig. 2. Monochromatic circular polarimeter for the measurements of the laser-induced birefringence based on the six-step phase-stepping method according to Patterson and Wang

2.3 Experimental protocol for retardance measurements

The optical retardation measurement consists in acquiring six images using a defined set of angles for the second quarter-wave plate (QWP2) (φ) and the half-wave plate (HWP) (β) while the first quarter-wave plate (QWP1) remains fixed at ρ = 135° (see Fig. 3 and Table 1). This protocol is based on the six-step phase-stepping method according to Patterson and Wang with an added half-wave plate as used in [21]. The acquisition process is fully automated using a homemade Python script that synchronizes the motors and camera acquisition while also handling retardation and stress map computation.

Table 1 Six-step acquisition method

Step	P1	QWP1 (ρ)	QWP2 (φ)	HWP (β)	P2
I_1	90°	135°	0°	22.5°	0°
I_2	90°	135°	0°	157.5°	0°
I_3	90°	135°	0°	0°	0°
I_4	90°	135°	45°	22.5°	0°
I_5	90°	135°	90°	45°	0°
I_6	90°	135°	135°	157.5°	0°

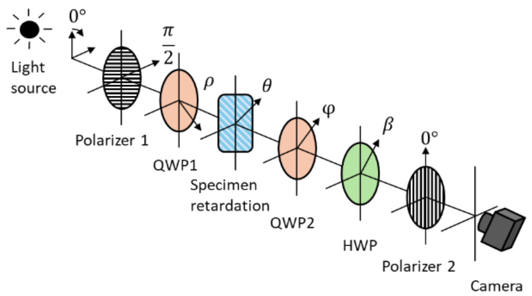

Fig. 3. Angular sequence for the six-step phase stepping method according to Patterson and Wang.

For each set of QWP2 and HWP angles, one image is acquired, resulting in six intensity frames $\{I_1, I_2, I_3, I_4, I_5, I_6\}$ per measured sample. Using the Mueller formalism and the computation of the transmitted Stokes vector, it is possible to calculate the isoclinic angle θ (1) and the optical retardation δ (2):

$$\theta = \frac{1}{2}\tan^{-1}\left(\frac{I_5-I_3}{I_4-I_6}\right). \tag{1}$$

$$\delta = \tan^{-1}\left(\frac{(I_5-I_3)\sin 2\theta-(I_4-I_6)\cos 2\theta}{I_1-I_2}\right). \tag{2}$$

From a practical point of view, a spatial filter (2 × 2 average block filter) is applied to reduce high-frequency noise on each image I_i before computing the retardation map. Moreover, the background, defined as the retardance map measured with two non-welded glass substrates, is subtracted from the retardance map obtained with the glass assembly (welded samples).

The system was carefully calibrated using a well-characterized quarter-wave plate and validated against numerical simulations based on the Mueller formalism (Fig. 4).

2.4 Birefringence and residual stress calculation

Based on the photoelastic model, the birefringence Δn (3) and the residual stress difference $\Delta\sigma$ (4) in the sample were calculated as follows:

$$\Delta n = \frac{\lambda\delta}{2\pi d}. \tag{3}$$

$$\Delta\sigma = \sigma_1 - \sigma_2 = \frac{\lambda\delta}{2\pi d C}. \tag{4}$$

where C is the photoelastic coefficient (3×10^{-6} MPa^{-1} [22,23]), λ is the wavelength of the light source, and d is the thickness of the laser-induced modification within the sample (the height of the bulk modification in our case). The calculation of the residual stress is based on the assumption that the birefringence in the sample is solely induced by the residual stresses in the sample.

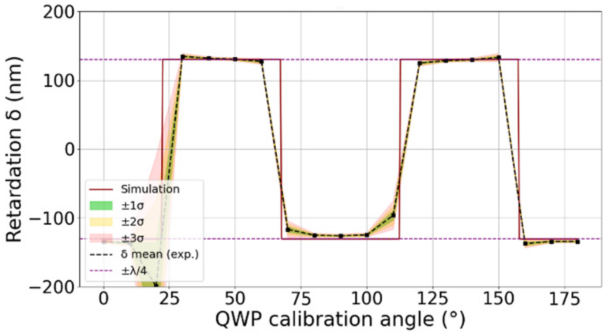

Fig. 4. Calibration of the circular polarimeter and the retardance calculation using Mueller formalism. The red line corresponds to the theoretical value whereas the black dashed line is the result of the experimental measurement, including spatial filtering and background correction.

2.5 Shear strength measurements

The shear strength measurements were carried out using a universal bench-top testing machine (Mecmesin, Omnitest 5 kN) equipped with a 5000 N sensor. The sensor precision is ± 25 N. A homemade sample holder was designed and implemented in order to apply only a shear force on the glass assembly (Fig. 5a), without any torsion contribution that may compromise the relevance of the measurements. As shown on Fig. 5b, the left part is fixed while the right is moving upward. So, the shear force is applied at the interface. This sample holder does not require any gluing for sample handling. A 1 inch assembly mounted in the sample holder is shown in Fig. 6 before and after the rupture.

The shear stress σ_{shear} is calculated as the ratio of the applied shear force F_{shear} over the welded area A:

$$\sigma_{shear} = \frac{F_{shear}}{A}. \tag{5}$$

As suggested in [18], when the welded area is far below the contact area, the calculation of the shear strength corresponding to the welded area σ_{shear}^{weld} has to take into account the contribution of both the welded area and the optical contact using the following formula:

$$\sigma_{shear}^{weld} = \frac{(F_w - F_{oc})}{A_w}, \tag{6}$$

where F_w is the measured force for a welded assembly, F_{oc} the measured force for optical contact only, and A_w the welded area.

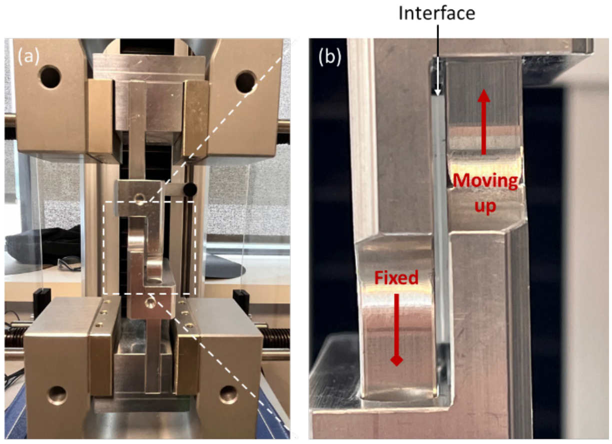

Fig. 5. Homemade sample holder for tensile shear tests of the glass assemblies (a) view of the device, and (b) loading configuration: the left part is fixed while the right part moves upward, applying a shear force at the interface.

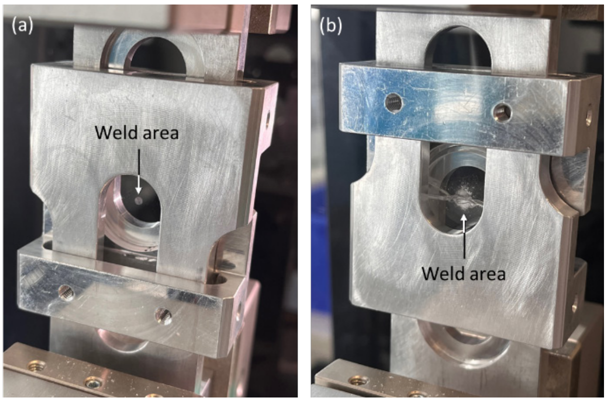

Fig. 6. Glass assembly in the sample holder (a) before and (b) after the rupture.

3. Results and discussion

3.1 Large-scale welding

Two fused silica samples with a thickness of 10 mm and a diameter of 2 inches each were welded in overlap configuration over a diameter of 45 mm using a spiral pattern with a pitch of 75 µm. The repetition rate was set to 200 kHz, the pulse energy to 51 µJ, and the scan velocity to 10 mm/s. As shown in Fig. 7, the weld seam is highly uniform across the entire surface of the welded area. A visual inspection with an optical microscope equipped with a 10x objective revealed no cracks and no instabilities along the weld seam. The antireflective coating is ablated into dust that is spread on both sides of the seam at the interface without any detrimental effect on the assembly. As explained in [24], the bubbles that are localized at the top of the bulk modification cause visible light scattering and consequently decrease the transparency of the welded area.

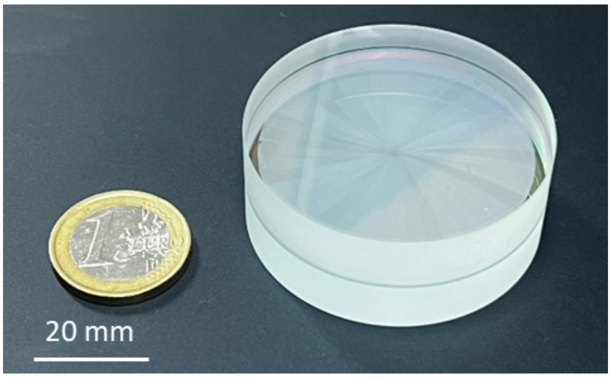

Fig. 7. Assembly of two fused silica samples with a thickness of 10 mm and a diameter of 2 inches with anti-reflective coating on both sides. The welded pattern is a full spiral with a diameter of 45 mm.

3.2 Shear strength measurements

Shear strength measurements were carried out on a batch of twenty assemblies, each consisting of two fused silica samples with a thickness of 3 mm and a diameter of 1 inch welded in overlap configuration using a full spiral pattern with a diameter of 2 mm (larger patterns do not break under a 5000 N load). Therefore, in such a configuration, the welded area A_w is 3.1 mm² meanwhile the optical contact area A_{oc} is 502.9 mm² (506 – 3.1 mm²). So, the ratio $\frac{A_{oc}}{A_w}$ is 161. Such a glass assembly is shown in Fig. 8a. The corresponding bulk modification extends on both sides of the interface (Fig. 8b). The bubble and the tip are far from the interface (more than 100 µm). The weld seam is crack-free and uniform across the welded area (Fig. 8c and 8d).

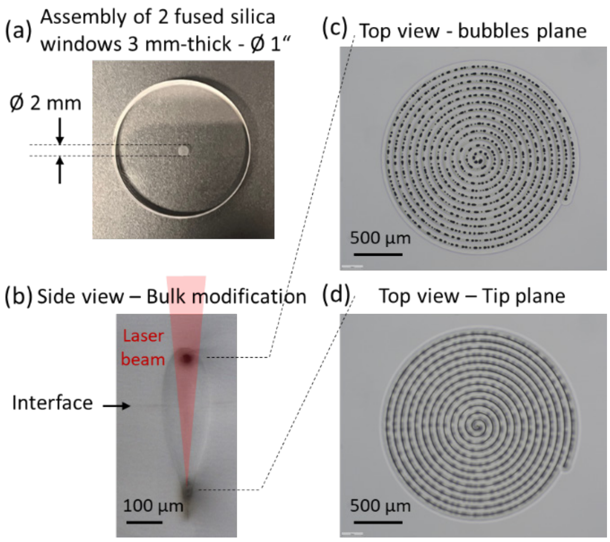

Fig. 8. (a) Assembly of fused silica samples with a thickness of 3 mm and a diameter of 1 inch used for the shear strength measurements; (b) Sideview of the bulk modification and its location relative to the interface; (c) Top view of the welded pattern in the bubbles plane; (c) Top view of the welded pattern in the tip plane.

Some preliminary measurements were performed with (i) a glass assembly, (ii) a steel dummy and (iii) an aluminum dummy, in order to assess the elastic deformation of both, the bench-top machine and the sample-holder under a heavy load (Fig. 9a). The three curves are similar. This behavior confirms that the measured deformation in Fig. 9a does not come from the sample but from the bench-top and the sample holder. Therefore, no conclusions about the deformation behavior of the welded sample itself can be drawn from the presented results, in contrast to the measured shear force and shear load values. The shear strength measurements were conducted under quasi-static loading conditions (displacement velocity 1 mm/min) and the sample holder was designed to result in no movement (or slippage) of the sample within the holder, as well as to result in a series load path (bench-top machine → sample holder → sample). Which means that a force equilibrium was present in the mechanical setup and that the sample was therefore subjected to the same force that was applied by the bench-top machine. Therefore, the measured shear forces and deduced shear loads are considered to be valid for the investigated samples, despite the elastic deformation of the sample holder and bench-top machine.

Some measurements were also performed on few samples solely joined through optical contact as a reference. The maximum load that can stand samples assembled solely through optical contact (F_{oc}) is 1834 ± 50 N, which corresponds to a shear strength value of 3.6 MPa. Nevertheless, the load drops down below 100 N if the optical contact is not perfect (when some Newton fringes are observed at the interface).

Conversely, ten samples assembled using laser welding broke before reaching the maximum load (5000 N) whereas ten others stand this load as shown in Fig. 9b. The values of F_w range from 900 to 5000 N (20 measurements). Four values are below the maximum measured force for pure optical contact of 1834 N (F_{oc}), and they were thus not considered for the calculation of shear strength (σ_{shear}^{weld}). Then, the shear strength (σ_{shear}^{weld}) is calculated using formula (6) for the 16 remaining measurements. The corresponding median endured shear stress of the welded area is about 1 GPa. A Weibull model is used to describe the probabilistic failure of glass assemblies that broke (only 6 samples). Fig. 10 describes the cumulative probability of the glass assembly failure as a function of applied shear stress. From this model we notice that the 50 %-risk of rupture is reached for a shear stress of 582 MPa as depicted in Fig. 10. This value is much higher than values formerly reported in the literature [2, 14, 17, 18].

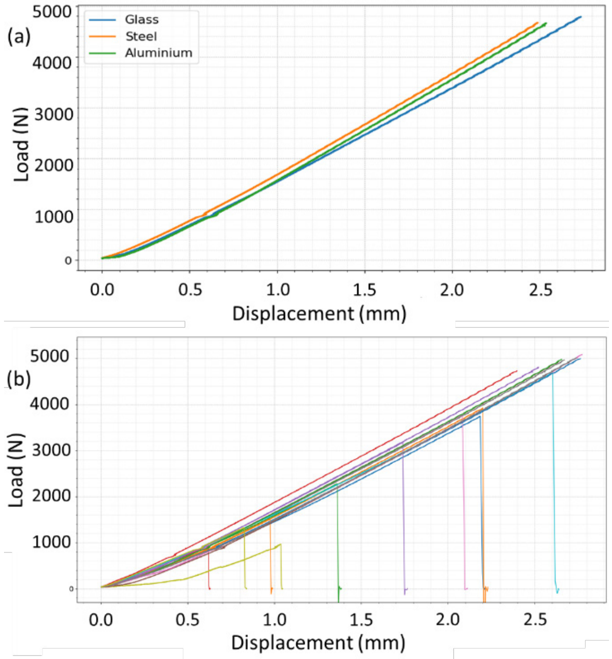

Fig. 9. Shear test load versus displacement (a) for 1 glass assemble, 1 steel dummy and 1 aluminum dummy, and (b) for the 20 samples of fused silica assemblies. Each vertical line corresponds to an assembly that broke.

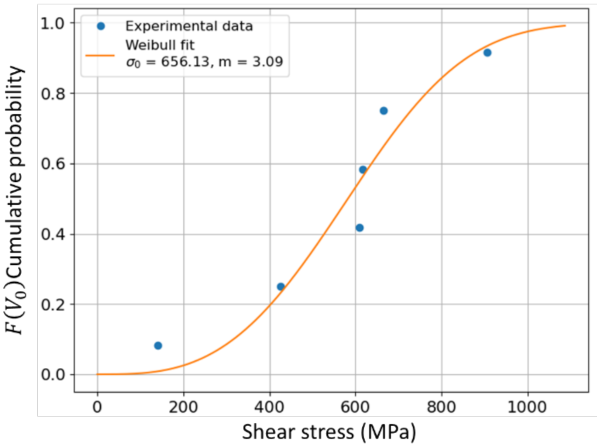

Fig. 10. Cumulative probability of rupture versus shear stress (MPa), i.e., Weibull distribution, for the 6 fused silica assemblies that broke during the shear test.

Fig. 11 shows micrographs of the center of a broken sample after shear strength measurements. Fig. 11(a) and Fig. 11(b) correspond to the upper glass substrate and the lower glass substrate, respectively. Both Figures indicate that the cracks are mainly located in the welded area on both substrates of the broken-assembly. Fig. 11(c) and Fig. 11(d) show a zoom located at the side of the welded pattern at the interface and 160 µm below the interface on the upper substrate, respectively. On Fig. 11(c) it is visible that only few cracks expand outward the welded area. The large one, on the left on the image, corresponds to the end of the laser trajectory which had been exposed to a high thermal gradient.

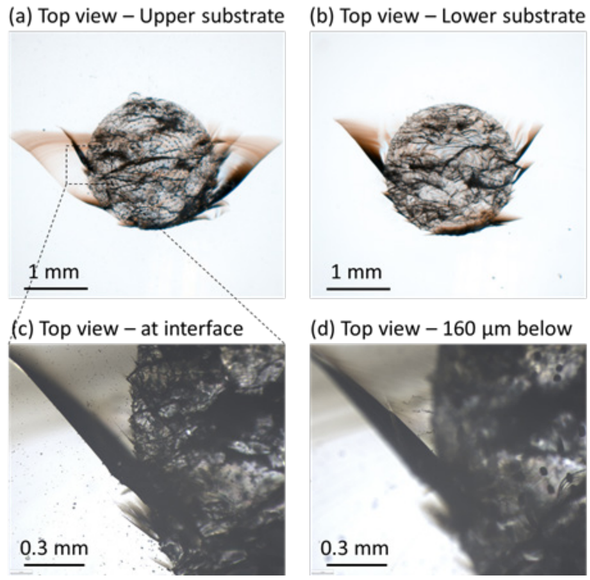

Fig. 11. Micrographs of a broken sample after shear strength measurements: welded area on upper substrate (a), welded area on lower substrate (b), zoom on the side of the welded pattern at the interface of the upper substrate (c), zoom on the side of the welded pattern 160 µm below the interface of the upper substrate (d).

These cracks may induce the rupture of the substrate along the sample diameter (not observed here). Moreover, we notice that some of these cracks propagate deep into the bulk material towards the bubble plane at a distance of 160 µm from the interface, as illustrated in Fig. 11(d). These observations demonstrate that the rupture of the glass assembly occurs in the welded area (over a 2 mm diameter spiral at the center), and not in optical contact area (outside the spiral).

3.3 Residual stress measurements

In order to assess the material integrity after transparent welding, some optical retardance measurements have been performed with a circular polarimeter in order to determine both laser-induced birefringence and residual stress. The results are shown in Fig. 12 for a full spiral pattern, and in Fig. 13 for an annular spiral pattern. These measurements were performed on 1-inch samples. Two interesting observations can be derived in particular from these measurements. First, the highest local variation of the optical retardance can be observed around the endpoint of the weld seam, also resulting in a high variation of the residual stresses (Fig. 12). This indicates a highly inhomogeneous material state in the region directly surrounding the end of the weld seam and therefore supports the assumption that the start-/endpoints of the trajectory are potential weak points, even if the absolute values of the measured residual stress do not directly appear there. Furthermore, virtually no optical retardance could be measured in the center region of the annular pattern, which was consequently observed to be free from any residual stress (Fig. 13).

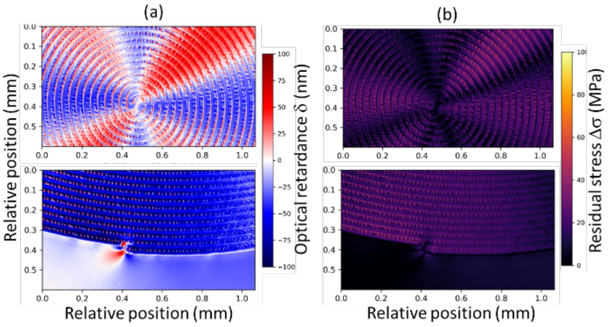

Fig. 12. (a) Optical retardance and (b) residual stress measured in fused silica in the center and at the end of the weld seam.

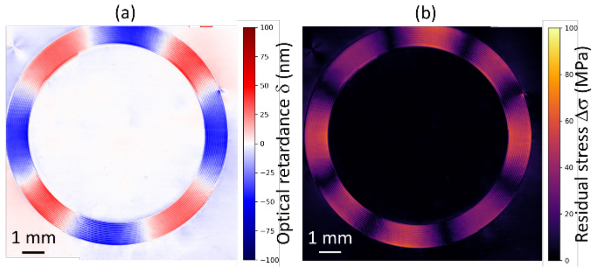

Fig. 13. (a) Optical retardance and (b) residual stress measured in fused silica for an annular spiral pattern.

3.4 Discussion

The high shear strength obtained after laser welding (section 3.2) results from a combination of several key factors. First of all, the set of parameters is chosen in order to minimize the thermal gradient and to induce a large and crack-free bulk modification as observed in Fig. 8(b). A high repetition rate (200 kHz) combined with a low scanning velocity (10 mm/s) corresponds to a high spatial overlap (83 %) between subsequent pulses which leads to heat accumulation and to enlarge the HAZ surrounding the energy deposition location. The resulting bulk modification has a teardrop shape as depicted in Fig. 8(b). Due to high temperature in the bulk modification, thermal decomposition of fused silica occurs, gas is released, and tiny bubbles appear in the bulk modification. These tiny bubbles migrate upward and aggregate into a larger one at the top of the bulk modification. Even if bubble formation can be avoided using high deposited energy [25], bubbles are present in our experimental conditions. Therefore, as shown in Fig. 8(b), the focus location should be set below the interface in order to place it more or less in the middle of the bulk modification at its maximum width (125 µm), and far from any defects such as the bubble at the top of the upper substrate or the tip-defect in the lower substrate.

Secondly, a spiral pattern enables to produce a continuous and stable welding seam along the laser trajectory as shown in Fig. 8(c) and Fig. (8d). Since the motion is achieved using XY-motorized stages the beam remains on the optical axis of the focusing lens, so there is no beam deformation along the laser trajectory, whatever the pattern dimensions (Fig. 7) rendering the process very robust. Moreover, the full overlap of the HAZ between subsequent turns in the spiral leads to a continuous, strong and defect-free bond that covers all the welded area. As observed in Fig. 11(c) and Fig. 12(a) the end of the laser trajectory is a weak point from which cracks can be initiated due to the high thermal gradient and propagate in the bulk outward from the welded area (see Fig. 11).

Finally, surface preparation and uniform clamping are crucial points. Any airgap at the interface should be avoided, otherwise residual tensile stress will appear and weaken the welded area. Moreover, it favours the optical contact which contributes to successful assembling since the shear strength decreases from 3.6 MPa to 0.2 MPa when Newton fringes are present. Uniform clamping avoids bending during the process and any additional residual stress in the glass assembly after laser treatment.

The shear strength resulting from the optical contact (3.6 MPa) is significantly below the shear strength of the welded area (median value is 1 GPa). The shear strengths of the welded area were calculated using eq. 6, which holds under the assumption that the area of and the corresponding shear force due to the optical contact are the same for the welded specimens and the specimens only under optical contact. The area calculations show that the welded area is negligeable compared to the optical contact area (ratio is 161). Furthermore, the reported shear force values F_{oc} for specimens only under optical contact were determined for samples showing no Newton fringes across the entire interface, indicating that the maximum possible surface of the specimens contributed to the optical contact. It is therefore assumed that these F_{oc} values represent maximum values for the contribution of the optical contact to the shear force, since the slightest decrease in contact area, as indicated by the appearance of Newton fringes, resulted in a significant reduction of the observed shear force (down to 100 N). The results of the shear strength obtained for the welded samples in this way can therefore be regarded rather as a lower bound of the shear strength of the weld seam. 16 out of 20 welded assemblies correspond to a maximum shear force well above F_{oc}. Thus, it can be concluded that most of the shear resistance comes from the welded area even if the optical contact covers an area 161 times larger than the welded area. This result demonstrates that transparent welding brings a significant reinforcement to optical contact, and therefore is highly relevant for glass assembly.

4. Conclusion

The presented paper reports on large-scale transparent welding of thick fused silica substrates using a femtosecond laser emitting 500 fs pulses at 1030 nm. The operating parameters were set in order to obtain an elongated and crack-free bulk modification and a stable weld seam. The welding pattern, either a full spiral or an annular spiral, was used to minimize the number of weak points along the laser trajectory. The pitch of the spiral was set to have a full HAZ overlap between two subsequent turns in the spiral. The process has been successfully applied on two fused silica samples with a thickness of 10 mm and a diameter of 2 inches, welded in overlap configuration over a diameter of 45 mm using a full spiral pattern. Tiny bubbles localized at the top of the bulk modification decrease the transparency of the welded area due to light scattering.

Shear strength measurements have been performed on a batch of 20 samples (with a thickness of 3 mm and a diameter of 1 inch), welded with a full spiral pattern of 2 mm in diameter, using a universal bench-top testing machine equipped with a 5000 N load sensor and a specific sample holder that does not require any gluing for sample handling and prevents any torsion constraints. Ten samples assembled using laser welding broke before reaching the maximum load (5000 N) whereas ten others stand this load. The contribution of the optical contact was considered for the calculation of the shear strength after laser welding. The median value of the endured shear stress on the welded area is about 1 GPa which is, to the best of our knowledge, far above the state of the art. Nevertheless, this value is five times below the theoretical shear stress value determined by Frenkel's estimation (4.9 GPa). Shear strength measurements of larger welding patterns than 2 mm in diameter were not performed since it requires a much stronger load sensor (above 5000 N).

Optical retardance has been measured using a monochromatic circular polarimeter and a six-step phase stepping method according to Patterson & Wang. From this, the residual stress was calculated based on the photoelastic model. The results indicate that the highest local variations of the residual stress are obtained at the endpoint of the welding trajectory. And more notably, the center region of the annular spiral pattern is free from any residual stress, which means that this pattern is highly relevant for optical component assemblies.

Therefore, this work paves the way to the assembly of large-scale optical components for high power laser manufacturing or for space photonics for instance.

Acknowledgments
The authors acknowledge (i) Matthieu Lancry, from Saclay University, France, and Jean-Pierre Guin from Institute of Physics of Rennes, France, for their support in mechanical characterization analysis.

References

[1] T. Tamaki, W. Watanabe, and K. Itoh: Opt. Express, 14(22), (2006) 10460.
[2] J. Sun, D. Li, S. Wan, J. He, Z. Bao, C. Sun, H. Jiang, J. Wang, K. Cao, Z. Wang, and H. Xu: Opt. Express 34(8), (2026) 14102.
[3] B. Ancelot, K. Mishchik, C. Javaux-Léger, J. Lopez, C. Hönninger, E. Mottay, and Rainer Kling: Proc. ICALEO, (2016) M408.
[4] S. Richter, S. Döring, A. Tünnermann, and S. Nolte: Appl. Phys. A, 103, (2011) 257.
[5] S. Richter, F. Zimmermann, A. Tünnermann, and S. Nolte: Opt. Laser Techn. 83, (2016) 59.
[6] I. Miyamoto, K. Cvecek, Y. Okamoto, and M. Schmidt: Appl. Phys. A, 114, (2014) 187.
[7] K. Cvecek, S. Dehmel, I. Miyamoto, and M. Schmidt: Int. J. Extrem. Manuf. 1, (2019) 042001.
[8] H. Yuan, C. Li, B. Yang, Y. Liu, Y. Cao, H. Jiang, H. Yang, X. Si, and J. Cao: Adv. Opt. Mat., 14, (2026) e01852.
[9] M. Lafargue, T. Guilberteau, P. Balage, B. Gavory, J. Lopez, and I. Manek-Hönninger: Materials, 18, (2025) 78.
[10] K. Mishchik, J. Lopez, G. Duchateau, B. Chassagne, R. Kling, E. Audouard, and E. Mottay: Proc LiM, (2017)
[11] A. Nakamura, M. Sakakura, Y. Shimotsuma, and K. Miura: J. Laser Micro Nanoeng., 12(2), (2017) 126.
[12] R. E. Mould, "The strength of inorganic glasses" ed. By L. J. Bonis, J. J. Duga, and J. J. Gilman (Springer, 1967) p.119.
[13] J. Frenkel: Z. Phys. 37, (1926) 572.
[14] I. Alexeev, K. Cvecek, C. Schmidt, I. Miyamoto, T. Frick, and M. Schmidt: Proc. LPM 2012, (2012).
[15] Y. Okamoto, I. Miyamoto, K. Cvecek, A. Okada, K. Takahashi, and M. Schmidt: J. Laser Micro Nanoeng., 8(1), (2013) 65.
[16] H. Chen, L. Deng, J. Duan, and X. Zeng: Opt. Lett 44(10), (2019) 2570.
[17] I. Miyamoto, K. Cvecek, Y. Okamoto, M. Schmidt, and H. Helvajian: Opt. Express 19(23), (2011) 22961.
[18] K. Cvecek, I. Miyamoto, J. Strauss, M. Wolf, T. Frick, and M. Schmidt: Appl. Opt. 50(13), (2011) 1941.
[19] D. V. Nelson: J. Phys. Photonics 3 (2021) 044003.
[20] E. A. Patterson and F. Wang: Strain, May (1991) 49.
[21] S. N. Hann, N. Macleod, P. O. Morawska, A. Dzipalski, R. M. Carter, I. Elder, R. A. Lamb, M. J. D. Esser, and D. P. Hand: Proc. SPIE, Vol. 11540, (2020) 115400W.
[22] E. Jog, R. Krishnan: Nature, 179, (1957) 540-541.
[23] K. E. Cramer, M. Hayward, and W. T. Yost: AIP Conf. Proc., 1581, (2014) 1679-1686.
[24] M. Lafargue: PhD thesis (2026), University of Bordeaux.
[25] E. Ofosu Kissi and Y. Bellouard: Opt. Expr. 26(11), (2018) 14024.

(Received: June 12, 2026, Accepted: September 13, 2026)